CRYSTAL GROWTH & DESIGN

Article

pubs.acs.org/crystal

Structural and Optical Emission Uniformity of *m*-Plane InGaN Single Quantum Wells in Core–Shell Nanorods

Emmanuel D. Le Boulbar,[*,∇,†,‡] Paul R. Edwards,[∇,§] Shahrzad Hosseini Vajargah,[∇,#,∥] Ian Griffiths,[⊥] Ionut Gîrgel,[†] Pierre-Marie Coulon,[†] David Cherns,[⊥] Robert W. Martin,[§] Colin J. Humphreys,[∥] Chris R. Bowen,[‡] Duncan W. E. Allsopp,[†] and Philip A. Shields[*,∇,†]

[†]Department of Electronic and Electrical Engineering and [‡]Department of Mechanical Engineering, University of Bath, Bath, BA2 7AY, U.K.

[§]Department of Physics, SUPA, University of Strathclyde, Glasgow G4 0NG, U.K.

[∥]Department of Materials Science and Metallurgy, University of Cambridge, Cambridge CB3 0FS, U.K.

[⊥]Department of Physics, University of Bristol, Tyndall Avenue, Bristol BS8 1TL, U.K.

ABSTRACT: Controlling the long-range homogeneity of core–shell InGaN/GaN layers is essential for their use in light-emitting devices. This paper demonstrates variations in optical emission energy as low as ~7 meV·μm^{-1} along the *m*-plane facets from core–shell InGaN/GaN single quantum wells as measured through high-resolution cathodoluminescence hyperspectral imaging. The layers were grown by metal organic vapor phase epitaxy on etched GaN nanorod arrays with a pitch of 2 μm. High-resolution transmission electron microscopy and spatially resolved energy-dispersive X-ray spectroscopy measurements demonstrate a long-range InN-content and thickness homogeneity along the entire 1.2 μm length of the *m*-plane. Such homogeneous emission was found on the *m*-plane despite the observation of short-range compositional fluctuations in the InGaN single quantum well. The ability to achieve this uniform optical emission from InGaN/GaN core–shell layers is critical to enable them to compete with and replace conventional planar light-emitting devices.

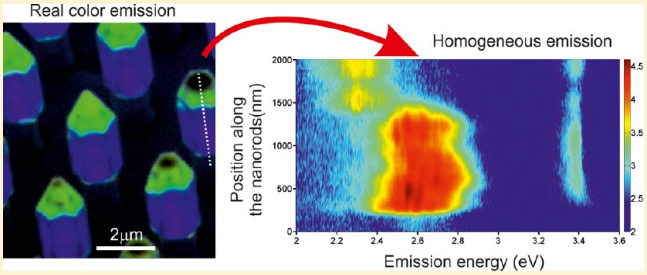

InGaN/GaN core–shell nanorod light emitting diodes (LEDs) have the potential to overcome the limitations of current-generation planar devices. Core–shell structures aligned along the [0001] *c*-axis can be grown with large-area {10$\bar{1}$0} *m*-plane sidewalls to create dominant nonpolar surfaces for growing LED structures, thereby eliminating the quantum confined Stark effect (QCSE) and its deleterious effect on the internal quantum efficiency, especially for wide quantum wells (QWs). The large surface area of high-aspect nanorods (NRs) brings the further advantage that carrier density in the active region is lower for a given injection current and so provides the scope to reduce efficiency droop.[1] In addition, core–shell LEDs also offer fast switching speeds due to the shorter carrier lifetimes in polarization-free structures for applications in short-range visible light communication.[2]

Realizing these advantages requires the formation of uniform InGaN/GaN QWs on the *m*-plane sidewalls of high-aspect-ratio NRs. However, the growth of such InGaN QWs on NRs often suffers from a gradient in InGaN composition and thickness along the nonpolar length of the nanorods.[3−6] While this phenomenon can be exploited for applications requiring broad absorption or emission bands, it will lead to strong emission wavelength shifts with drive current. More homogeneous emission is required in LEDs than has been reported, and the current literature suffers from a lack of correlation between the structural and the optical properties of the core–shell structure.

GaN cores can be obtained by bottom-up epitaxial growth or top-down etching of planar layers. Several approaches have been used to grow bottom-up NRs: vapor–liquid–solid (VLS) growth, involving a catalyst droplet to trigger the vertical or oblique growth;[7,8] self-assembled growth, requiring particular growth conditions such as low V/III ratio, silane doping or high temperature in order to enhance the vertical growth on nucleated GaN islands;[9−12] and selective area growth, either combined with a pulsed-growth mode,[4,13] or via continuous-flow growth.[14] Homogeneous GaN NR arrays have been obtained using selective area growth combined with a pulsed-growth mode,[15] or via continuous-flow growth on either N-polar[16−18] or Ga-polar substrates.[19−21] These methods have the advantage of producing defect-free NRs beyond the initial nucleation step. The top-down approach, while creating the cores from defective planar templates, has the benefit of giving rise to highly uniform GaN NR arrays as a result of controlled etching and facet regrowth processes.[22] This is advantageous for fabricating devices with higher yield and easier scalability to

Received: October 8, 2015
Revised: February 24, 2016
Published: March 7, 2016

DOI: 10.1021/acs.cgd.5b01438
Cryst. Growth Des. 2016, 16, 1907−1916

production systems by reducing the demanding requirements of a bottom-up growth process. It is important to note that etched GaN nanorods, depending on their diameter and density, can also be free of dislocations.[23]

This paper reports quantitative structural and optical studies on InGaN/GaN core−shell structures grown on etched NR arrays. Long-range optical emission and structural uniformity of the InGaN *m*-plane QW was achieved on a 2000 nm pitch hexagonal NR array. Previous work showed that InGaN growth on the sidewalls of tall (4000 nm high), 400 nm diameter GaN nanorods with a 600 nm pitch resulted in a decreasing InN-incorporation on their *m*-plane sidewalls from top to bottom.[24] Therefore, the NR array geometry and pitch are useful parameters for optimizing the epitaxial growth of GaN/InGaN core−shell structures. The results reported here demonstrate that QW uniformity is not a limiting factor for this device architecture.

EXPERIMENTAL SECTION

GaN/AlN/Si NR arrays on silicon were fabricated using a top-down approach from conventional *c*-plane GaN-on-silicon templates grown by metal organic vapor phase epitaxy (MOVPE). The total III-nitride thickness, including AlN-based nucleation and alloy grading layers, was ∼1.8 μm. Further information on sample fabrication and preparation can be found in the Experimental Details. The scanning electron microscopy (SEM) image in Figure 1 shows a cross-section through the GaN/AlN/Si NR array after plasma etching. The template has been etched completely through the III-nitride layers into the Si substrate.

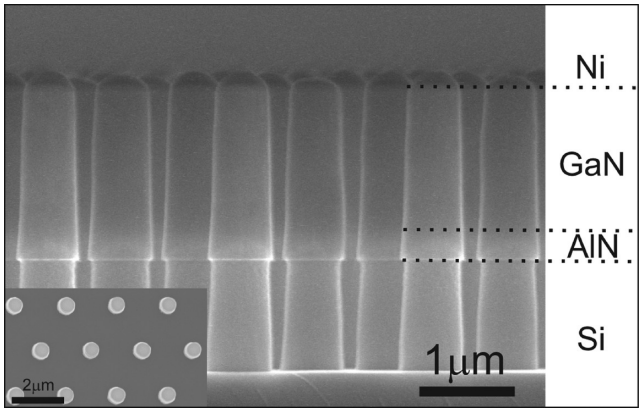

Figure 1. Planar and cross-section SEM images of etched GaN NR arrays.

Because of the physical etching and ion bombardment, the NRs are slightly tapered and suffer from sidewall roughness. It is therefore necessary to recover a smooth GaN surface using a GaN epitaxial regrowth step prior to subsequent growth of the InGaN layer.[22] The result of this first growth step is to produce faceted NRs typically bound by $\{10\bar{1}0\}$ and $\{10\bar{1}1\}$ planes with the latter intersected by a (0001) plane if the NR is truncated. If the starting GaN template is grown on a Si substrate, Ga melt-back etching of the latter must be avoided to achieve selective growth on the III-nitride surfaces only. Consequently, the etched NR array was first subjected to a high-temperature annealing (1050 °C) in NH_3 atmosphere to achieve thermal nitridation of the Si surface.

The morphology of the GaN/AlN/Si NR array after GaN overgrowth is shown in the SEM images of Figure 2 where it can be seen that growth only occurs on the exposed III-nitride surfaces. Further, the lateral steps and absence of obvious faceting on the AlN-containing layers indicate that the lateral overgrowth on these layers is substantially lower than on the GaN section of the NRs. After the GaN

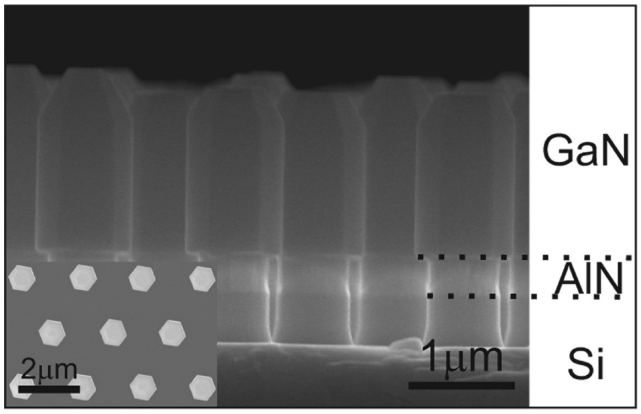

Figure 2. Planar and cross-section SEM images of faceted GaN NR arrays.

overgrowth step, the NR morphology can be clearly resolved, consisting of six smooth *m*-plane facets $\{10\bar{1}0\}$, six semipolar facets $\{10\bar{1}1\}$, and a *c*-plane facet (0001) truncating the top pyramidal nanostructure.

Three samples of the faceted GaN NRs were then overgrown with an InGaN shell at temperatures of 750, 700, and 650 °C respectively, followed by a GaN capping layer that is identical in all three samples. Further growth parameters can be found in the Experimental Details.

RESULTS AND DISCUSSION

Analysis of the structural properties of the InGaN shells involved performing cross-sectional scanning transmission electron microscopy (STEM)[25] and energy dispersive X-ray (EDX) spectroscopy.[26]

Figure 3a shows a reconstruction of multiple high-angle annular dark-field (HAADF) STEM images, taken along the $[11\bar{2}0]$ direction, stitched together in order to show a complete set of facets of the GaN/InGaN core−shell. The structure shown in Figure 3a was grown at 650 °C and is typical of the sample set. Examples of individual images for three critical positions on the *m*-plane (top, middle, and bottom) are shown in Figure 3b−d.

The thickness of the InGaN layer was found to differ from one facet to another. Starting at the top of the NR, the layer thickness was 20 nm on the residual (0001) *c*-plane, 8 nm on the upward facing $\{1\bar{1}01\}$ semipolar facet, between 10 and 11 nm on the $\{10\bar{1}0\}$ *m*-plane and 11 nm on the downward facing $\{\bar{1}101\}$ semipolar planes. In comparison to QWs in a conventional *c*-plane MQWs LED, all can be classified as a wide single quantum well (SQW), being wider than the expected exciton Bohr radius.[27] Although not resolvable in Figure 3, accurate measurements of the InGaN SQW thickness, obtained every 20 nm along the entire 1200 nm length of the *m*-plane, reveal a slight increase of the thickness from the bottom to the top, from 10 to 11 nm up the NR. This 10% increase compares well with the 14% gradient of thickness reported elsewhere for a similar GaN/InGaN structure grown on a sparser GaN NR array.[28] Figure 3d, obtained from the lower part of the NR, also indicates an aggregation of InGaN at the interface between the etched AlN and the −*c*-plane. The thickness of the GaN cap layer was very thin, approximately 1 nm on the semipolar $\{10\bar{1}1\}$ plane and about 7−8 nm on the *m*-plane.

Atomic resolution images obtained of the *m*-plane InGaN/GaN QW grown at 700 °C provided no evidence that dislocations are formed at the interfaces. A representative image

DOI: 10.1021/acs.cgd.5b01438
Cryst. Growth Des. 2016, 16, 1907−1916

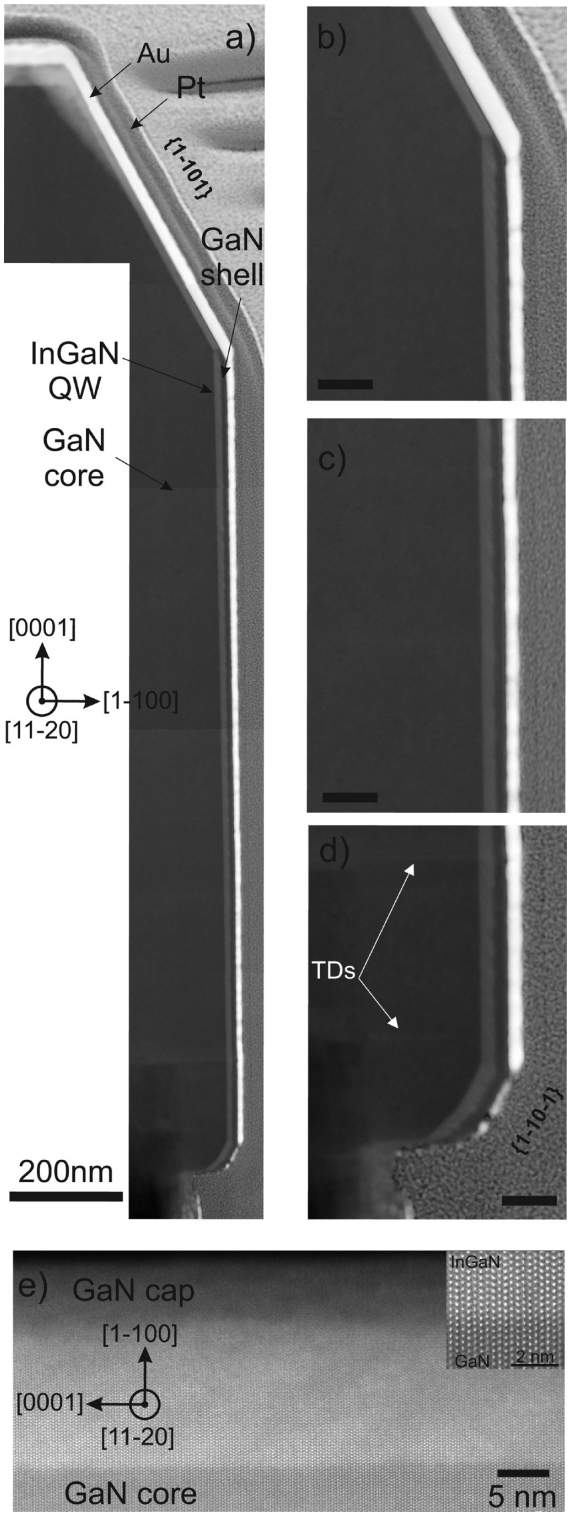

Figure 3. (a) HAADF STEM image[25,26] reconstruction of the radial InGaN/GaN core−shell structure grown at 650 °C showing the homogeneous thickness of the InGaN well from top to the base. Images showing (b) the interface between semipolar and nonpolar *m*-plane (c) the middle, and (d) the base of the NR. (e) Atomic resolution image of the *m*-plane InGaN/GaN interface for the sample grown at 700 °C. The inset shows a magnified image of the interface between the GaN core and the InGaN QW. Scale bars in (b−d) are 50 nm. Images were taken along the [11$\bar{2}$0] direction.

is shown in Figure 3e. Thus, while the etched cores may contain threading dislocations, the regrowth process appeared not to introduce new dislocations that could reduce the lifetime of carriers in the QW.

Further examination of the HAADF images shows that the morphology of the InGaN layers is strongly dependent on the growth facet. This can be seen most clearly in Figure 3b, showing the intersection between the {1$\bar{1}$01} plane and the *m*-plane. The {1$\bar{1}$01} plane SQW remains smooth, whereas the outer surface of the *m*-plane appears somewhat roughened. This was a feature of both 700 and 650 °C samples.

The InGaN alloy composition within the SQWs was examined by EDX spectroscopy.[26] Figure 4 shows typical

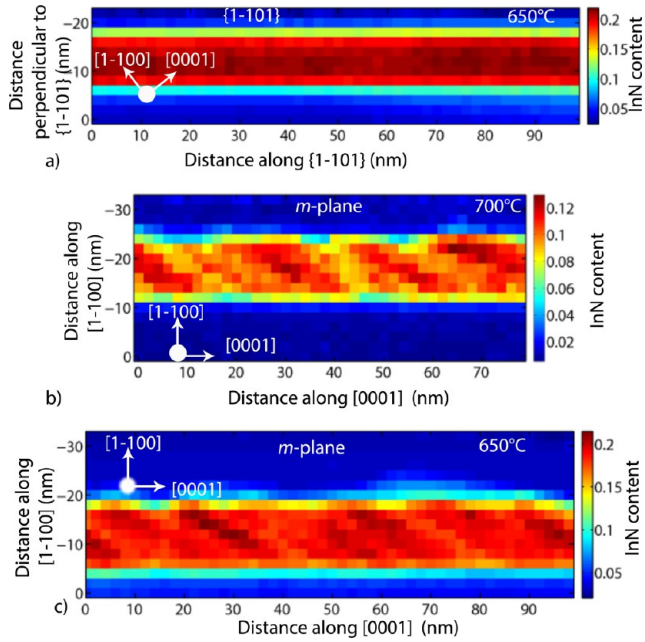

Figure 4. Indium map of the wide InGaN SQW obtained by EDX on (a) {1$\bar{1}$01} plane at 650 °C, (b) *m*-plane at 700 °C, and (c) *m*-plane at 650 °C growth.

EDX maps of the InN fraction for the {1$\bar{1}$01} and *m*-planes for the samples grown at 650 and 700 °C. They clearly reveal the facet-dependence of the InN fraction and the relative degree of homogeneity. These EDX maps show that the InGaN SQW on the {1$\bar{1}$01} plane is uniform in both the in-plane and cross-well directions, whereas this is not the case for the *m*-plane SQW. Both facets show a degree of grading at the lower interfaces, likely as a result of the resolution and misalignment of the electron beam. At the upper interfaces, the alloy grading of the {1$\bar{1}$01} plane is similar to the lower; however, there is a marked increase in the compositional fluctuation at the upper interface of the *m*-plane. This correlates with the roughening of the outer interface of the *m*-plane SQW observable in Figure 3b,c.

The lack of roughness on the {1$\bar{1}$01} plane SQW indicates that the growth mechanism is not the same as on the *m*-plane. The {1$\bar{1}$01} planes evolve by a self-limiting process during the initial GaN facet recovery growth step performed after etching the NR cores, whereas the *m*-planes evolve from the slightly tapered etched NR sidewalls. Incomplete recovery of the *m*-planes from the tapered side-walls is equivalent to a slight miscut which could lead to a modification of the InN composition and dual emission.[29,30] Other factors that could contribute to the roughness of the InGaN shell include facet-dependent

DOI: 10.1021/acs.cgd.5b01438
Cryst. Growth Des. 2016, 16, 1907−1916

variations in the indium sticking coefficient and pseudomorphic strain. There is also evidence for increased InN incorporation at the apexes between the facets, such as between $\{1\bar{1}01\}$ and *m*-plane. Understanding the complexity in the InGaN shell growth is the subject of ongoing investigation.

From an applications perspective, the longer range variations in InN fraction of the SQW are important. Therefore, the variation of InN content along the length of the rod was examined by taking EDX maps from near the top, middle, and base of the *m*-plane facet and by comparing the average values within each map. Quantatitive analysis of the InN fraction down the length of the *m*-planes was achieved by creating cross-well average profiles from 80 to 100 nm segments at the different positions along the *m*-plane. This process resulted in the formation of radial profiles of the average InN mole fraction (see sketch in Figure 5a) at the top, middle, and bottom of a typical core−shell NR, to provide a test for the long-range uniformity of the InN mole fraction rather than its local homogeneity.

Each row of pixels within the map was statistically analyzed to provide the average as well as the standard deviation as a measure of the uncertainty. Figure 5b shows cross-well profiles of the InN fraction in the SQW grown at 700 °C formed on the *m*-plane measured at three different positions along its length. Within experimental error the profiles lie on top of each other, thus demonstrating the uniformity of the locally averaged InN fraction down the entire length of the *m*-plane facet. Figure 5c shows the same is true for the sample grown at 650 °C.

As a comparison, Figure 5d shows the cross-well profile for the semipolar $\{1\bar{1}01\}$ facets measured at two locations for the sample grown at 650 °C. The data confirm the result in Figure 3 that the SQW formed on the $\{1\bar{1}01\}$ facets is narrower than that formed on the *m*-planes. However, the InN incorporation on the $\{1\bar{1}01\}$ planes is higher at 21.5 atom % (peak value) compared to 18.6 atom % on the *m*-plane in the 650 °C sample. The change of InN content with decreasing temperature on the $\{1\bar{1}01\}$ planes from 18.5 to 21.5 atom % is less pronounced than on the *m*-plane (10.3−18.6 atom %), but is similar to previous observations by Wernicke et al., which imply a saturation of InN fraction with reducing growth temperature, albeit at higher values of ∼30 atom %.[31] This could be explained by the use in this work of TMGa rather than TEGa, since it does not decompose as efficiently at low temperature.

The estimated long-range variation in spatially averaged InN fraction along the *m*-plane is ∼0.4 atom % and lies within the experimental errors. This can be compared with the estimated short-range variations of ∼2 atom % and ∼2.5 atom % for 700 and 650 °C respectively, due to the In-rich fluctuations observable in Figure 4b,c. As such, the fabrication process reported here has resulted in the formation of InGaN/GaN SQW core−shell structures in which the *m*-plane optical properties are likely to be more governed by the local, nanoscale properties of the SQW rather than by the vertical gradients in the InN mole fraction along the vertical axis of the NRs.

The uniformity of the optical emission of the GaN/InGaN/GaN core−shell structures was assessed by room-temperature high-resolution cathodoluminescence (CL) hyperspectral imaging.[32] The measurement conditions can be found in the Experimental Details. The secondary electron images in Figure 6a−c shows the field of view and measurement geometry for the CL hyperspectral data sets obtained. The mean cathodoluminescence spectrum for the whole field of view for

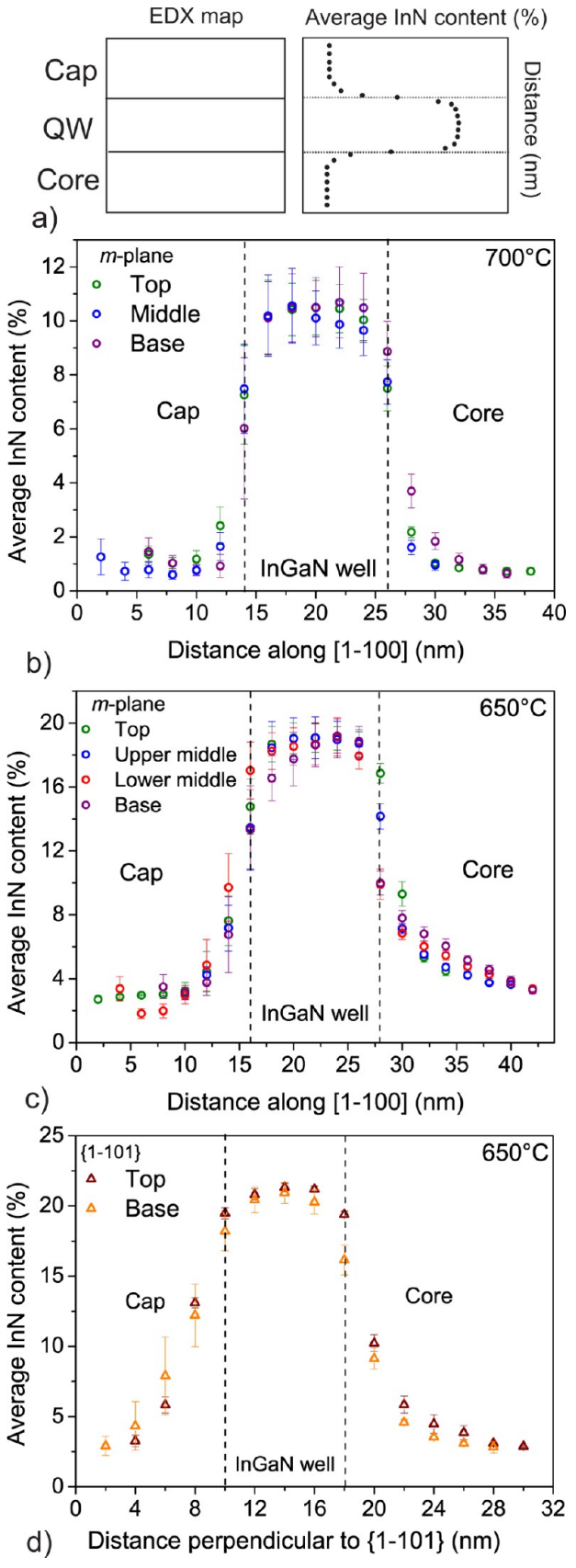

Figure 5. (a) Sketch representing EDX map to graph transformation. Locally averaged InN contents measured using EDX at different positions along the *m*-plane facets grown at (b) 700 °C and (c) at 650 °C and along the $\{1\bar{1}01\}$ facet grown at 650 °C.[26]

DOI: 10.1021/acs.cgd.5b01438
Cryst. Growth Des. 2016, 16, 1907−1916

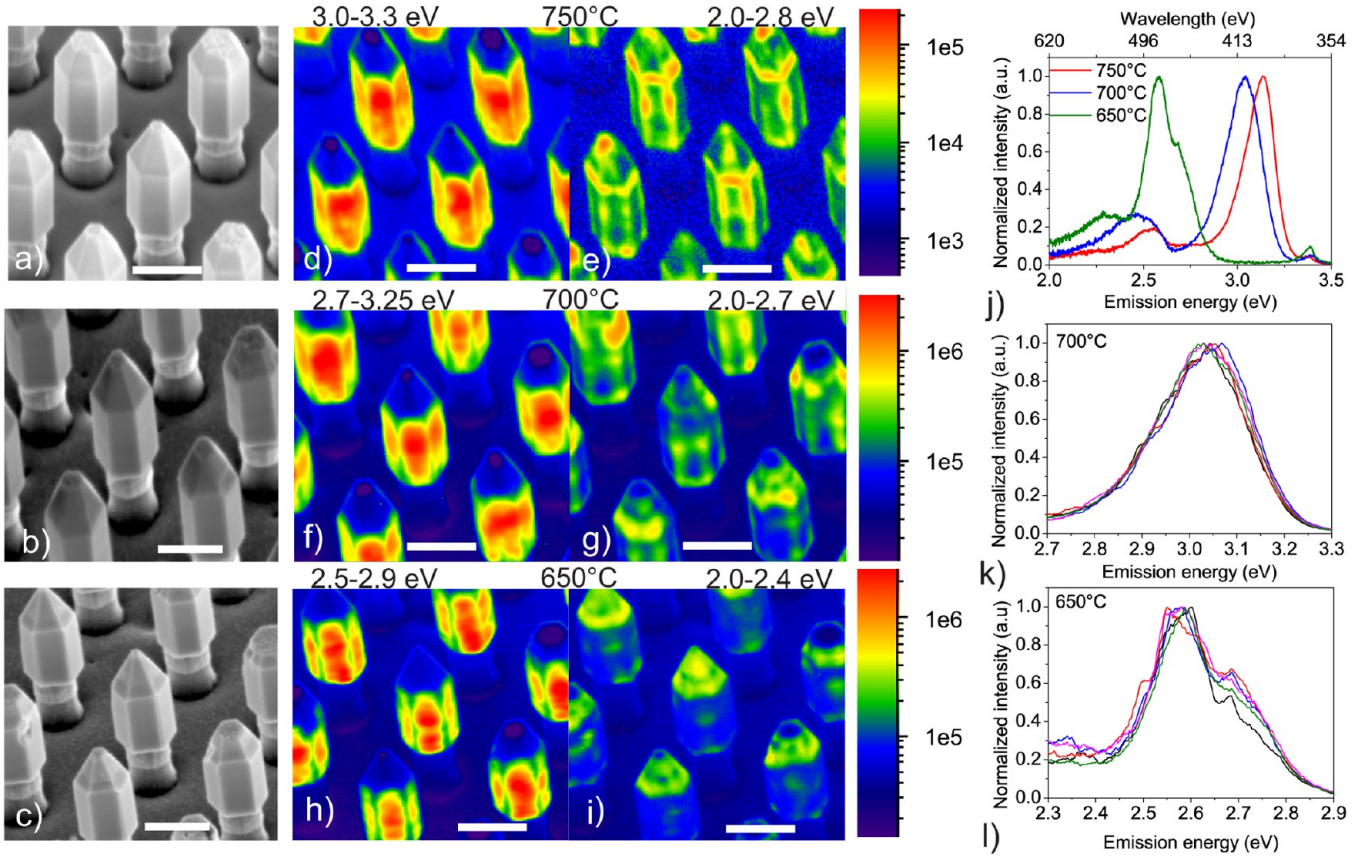

Figure 6. (a–c) SEM images of GaN/InGaN/GaN core–shell structures grown at (a) 750 °C, (b) 700 °C, and (c) 650 °C. (d–i) Log-scale CL intensity images extracted from the hyperspectral data set over different spectral ranges: (c–d) 3.0–3.3 eV and 2.0–2.8 eV for the sample grown at 750 °C, (e–f) 2.7–3.25 eV and 2.0–2.7 eV for the sample grown at 700 °C, and (g–h) 2.5–2.9 eV and 2.0–2.4 eV for the sample grown at 650 °C. (j) Area-averaged, room-temperature CL spectra from the three samples. (k–l) *m*-plane emission peak of multiple individual nanorods for samples grown at (k) 700 °C, and (l) 650 °C. Scale bars are 1 μm.

the three samples grown at different InGaN growth temperatures is shown in Figure 6j. Two separated peaks can clearly be distinguished in each spectrum, with the more intense peaks being centered at 3.13, 3.05, and 2.63 eV, and the lower intensity peaks centered at 2.55, 2.45, and 2.30 eV for the samples grown at 750, 700, and 650 °C, respectively. The decrease in growth temperature led to a clear red-shift of both peaks, as expected from the increase in the InN fraction with decreasing growth temperature found from the EDX measurements.

Integrating over each of these main peaks within the CL data set allows maps to be generated that show the origin of the luminescence peak. These are shown in Figure 6d–e for the two peaks in the 750 °C sample, Figure 6f–g for the 700 °C sample and Figure 6h–i for the 650 °C sample. By examining the spatial dependence of the emission, it can be seen that the higher-energy emission peaks arise from the *m*-plane, while the lower-energy peaks arise both from the $\{1\bar{1}01\}$ plane facets and from the facet intersections, both *m*-plane–*m*-plane and $\{1\bar{1}01\}$ plane–*m*-plane (Figure 6c–i). Emission arising from the *m*-plane was always found to be brighter than that from either $\{1\bar{1}01\}$ plane facets or apexes.

Several factors can contribute to the weaker intensity emission from the semipolar plane. These include the presence of the QCSE, nonoptimum growth conditions for this InN fraction and the higher number of structural defects that have been reported in similar structures.[6] There are a number of explanations for the lower-energy emission observed at the apexes; first it is possible that between the *m*-planes very small *a*-plane facets have been created which have been shown to emit at lower energy than the corresponding *m*-plane,[33] though this is not seen in the SEM images. Second, strain relaxation will occur at the apexes, which can lead to the preferential integration of InN,[34] as well as a reduction of the lattice deformation contribution to the fundamental energy band gaps of the materials comprising the local SQW.[35,36]

In order to understand the further factors contributing to the line shape of the emission from the *m*-plane facets, the normalized emission from the *m*-planes of several different nanorods within the field of view are shown in Figure 6, panels k and l at 700 and 650 °C respectively. This figure shows that *m*-plane emission from NR to NR is very uniform, and that the shape of the emission peak arises from effects within individual NRs.

Figure 7 shows spectral line-scans (extracted from the same CL data sets) along the length of an individual GaN/InGaN NR, with the luminescence intensity plotted on a logarithmic scale. The zero nm position represents the bottom of the AlN layer and the 2000 nm position, the top of the nanorod. On all figures, a clear interface is seen at the 200 nm position, corresponding to the AlN and GaN interface. (Note that the scale on the *y*-axis takes account of the tilted sample geometry seen in Figure 6a–c.) A room-temperature, wurtzite GaN band edge emission around 3.4 eV[37] is observed all along the NR for

DOI: 10.1021/acs.cgd.5b01438
Cryst. Growth Des. 2016, 16, 1907–1916

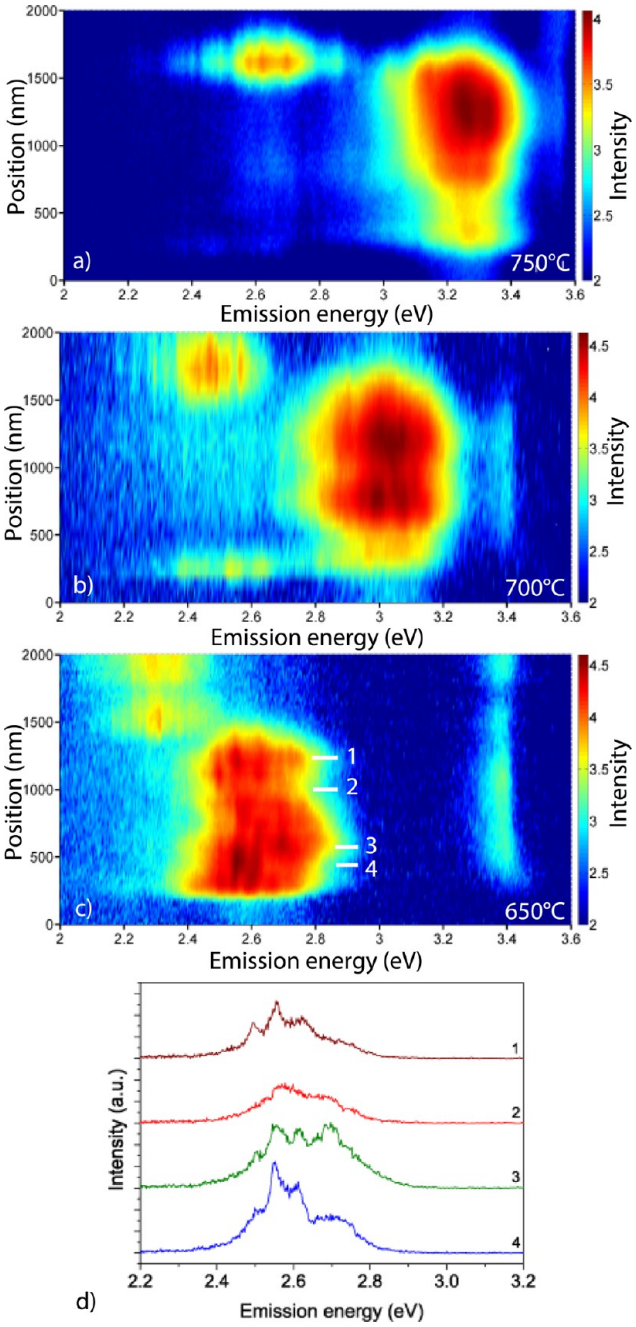

Figure 7. Log−scale room temperature CL spectra as a function of the position along GaN/InGaN nanorod for growth temperatures of (a) 750 °C, (b) 700 °C, and (c) 650 °C. (d) Individual spectra from different positions along the *m*-plane of a single nanorod from the 650 °C sample. The spectra correspond to positions 1, 2, 3, and 4 from (c) and show the effect of resonances on the emission from different points of the *m*-plane.[32]

both samples grown at 700 and 650 °C. On the *m*-plane facet, from the top of the AlN layer at 200 nm to the base of the nanopyramid at 1400 nm, a homogeneous emission band is found for every growth. Note that the uniformity in the light emission reported here is greater than most results reported in the literature, where a shift in the emitted photon energy as a result of a gradient in indium composition is often found,[5,38] for example, by as much as 230 meV·μm^{-1}.

The weaker emission found at the base of the nanorod can be explained by the higher number of dislocations expected in this region. An indication of this can be seen in the contrast in the HAADF STEM image in Figure 3d where lines (indicated by white arrows) can be seen propagating from the core toward the *m*-plane.

Within the *m*-plane emission band resonances can be observed (dark red at 2.58 eV in Figure 7c) due to optical cavity modes (either whispering gallery or Fabry−Perot) which arise due to the nanorod geometry.[39] Individual spectra taken along the linescan (Figure 7d) show resonances appearing and disappearing along the length of the NR. The presence of these optical resonance modes in the CL spectrum makes it difficult to observe any underlying gradient in the energy of emission from the *m*-plane. To overcome this, we instead calculate the centroid energy over the energy range of this *m*-plane emission peak to provide a statistical measure of any shift in the peak.[40] This was calculated for a line-scan on each of the complete nanorods displayed in Figure 6 and is shown in Figure 8 against distance along the *m*-plane facet. For an individual nanorod the centroid energy oscillates, most likely due to the different cavity modes that come into and out of resonance. Neighboring nanorods have a similar overall dependence, but can have different sets of resonances. This leads to a set of oscillatory energies surrounding a linear mean dependence with distance, represented by the dashed lines in Figure 8. These lines indicate that the emission shifts to higher energy closer to the bottom of the nanorods, and this shift is more pronounced as the temperature decreases, from 7 meV·μm^{-1} at 750 °C to 36 meV·μm^{-1} at 700 °C to 40 meV·μm^{-1} at 650 °C. The cause of this shift is likely due to gas-phase diffusion on which the growth of InGaN on three-dimensional structures is expected to depend, whereby increased diffusion of the In precursors at the higher temperatures leads to an increase in the uniformity.

The optical emission energy from InGaN/GaN-based QWs will be determined by the bandgap of the InGaN well, the electron and hole confinement energies and any red-shift caused by the QCSE. For the nonpolar *m*-plane, there is no polarization field; therefore the QCSE is zero. An upper limit for the confinement energies can be obtained from the simple infinite QW model, $E = \hbar^2\pi^2/mL^2$, using electron and hole effective masses of $m_e^* \approx 0.2m_0$ and $m_h^* \approx 0.8m_0$ and L being the thickness of the SQW. This gives a total confinement energy of ∼24 meV for a 10 nm QW. Measurements of the QW width using HAADF STEM show the thickness changing from 10 to 11 nm along the ∼1 μm high *m*-plane. This variation is calculated to have only a small effect on the QW confinement energies on the order of a few meV and can be neglected with regard to the centroid emission energy variation, which is significantly greater, at around 50 meV as shown in Figure 8.

By combining the average optical emission peak energy of the *m*-plane from cathodoluminescence (Figures 6 and 8) and the corresponding average m-plane InN mole fraction for the center of the QW from EDX (values from Figure 5), one can compare the results with a modified Vegard's law using published values of the bowing parameter. Orsal et al. determined values of the bowing parameter, *b*, from InGaN samples with InN fraction ranging from 0 to 25 atom % and thicknesses of 10−200 nm, and found values of $b = 1.32 \pm 0.28$ and $b = 2.87 \pm 0.20$ for strained and unstrained InGaN, respectively.[41] The calculated bandgap versus InN mole fraction curves are shown in Figure 9 alongside the two experimental data points from the nonpolar *m*-plane for the two samples grown at 700 and 650 °C, as determined by CL

DOI: 10.1021/acs.cgd.5b01438
Cryst. Growth Des. 2016, 16, 1907−1916

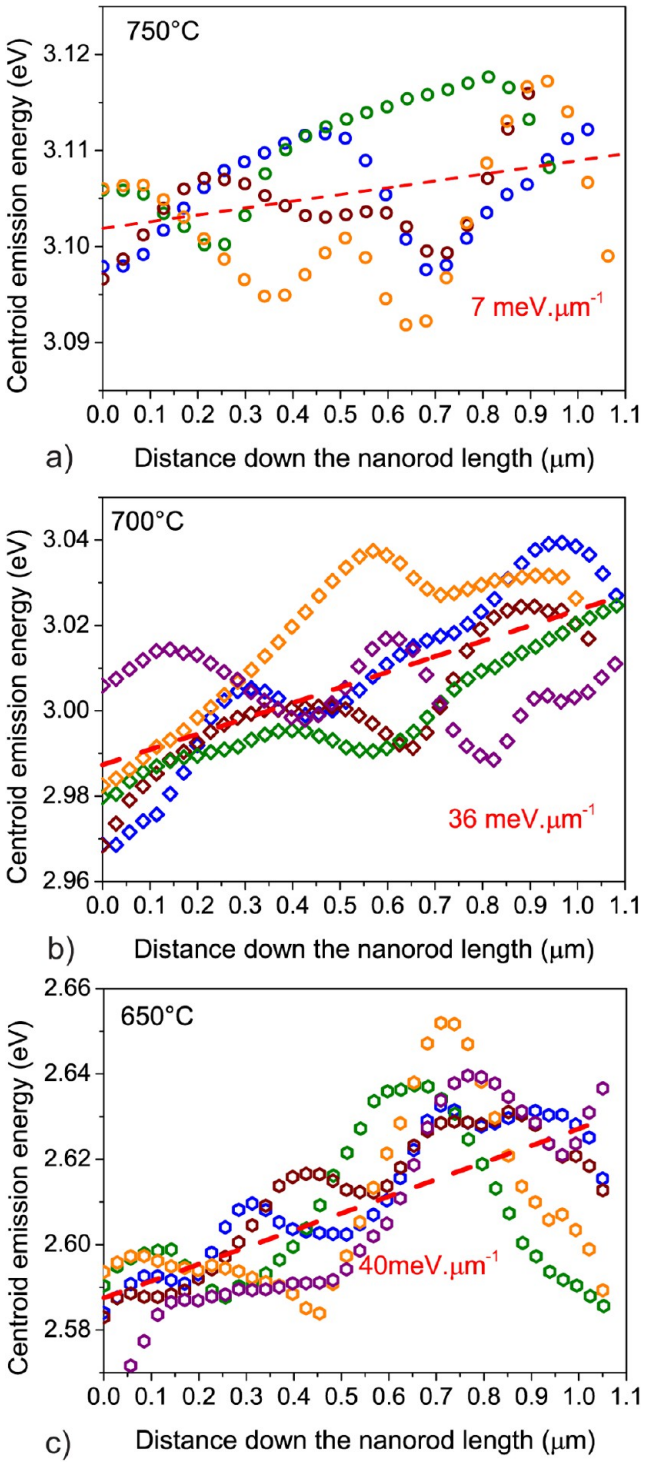

Figure 8. Room temperature centroid emission energy measured down the length of several nanorod *m*-plane fac-ets by averaging 5 pixels perpendicular to the linescan for growth at (a) 750 °C, (b) 700 °C, and (c) 650 °C. The dashed lines represent the linear fit obtained from the mean of 4−5 nanorods. The top of the *m*-plane is toward the left of the figure.[32]

and EDX as described above. The results in Figure 9 indicate that the QW grown is partially relaxed.

Comparing with the literature, strain measurements of $In_xGa_{1-x}N$/GaN core−shell NRs with $x \approx 30$ atom % showed that they are almost fully strained for a thickness of 9 nm, whereas they are plastically relaxed through the generation of

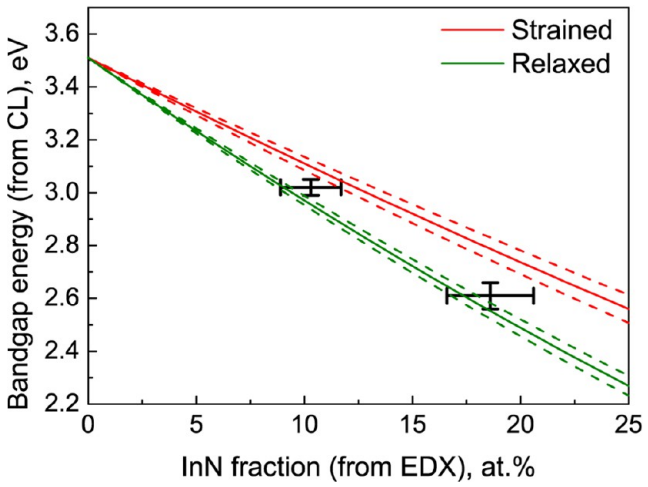

Figure 9. Locally averaged *m*-plane InN fraction measured by EDX as a function of CL emission energy for 700 and 650 °C compared with a modified Vegard's law equation for strained and relaxed layers.[42] The dotted lines represent Vegard's law obtained for the highest and lowest estimated values of *b*.

misfit dislocations for a thickness of 23 nm.[34] In contrast, the data in Figure 9 imply our structures are partially relaxed for lower InGaN layer thicknesses and InN fraction.

As no misfit dislocations were found through TEM analysis, it is unlikely that strain relaxation in the InGaN layer has occurred via plastic deformation, rather by elastic relaxation. An alternative explanation for the data in Figure 9 could be that the CL emission originates from the InN-rich regions within the QW. This would mean that the experimental data points would shift to higher InN fractions by an amount reflecting the magnitude of the short-range variations, ∼2−2.5 atom % as stated previously. Using half this peak-to-peak value for an estimate of the shift from the mean value currently used in Figure 9, the datum at 10.3% corresponding to the sample grown at 700 °C would shift to 11.3 atom %, and the datum at 18.6 atom %, grown at 650 °C would shift to 19.9 atom %. These shifts bring the data points closer to the line corresponding to Vegard's law for strained layers, but the conclusion that the QW is partially relaxed would still stand, at least for the sample grown at 650 °C. More investigation is required to determine the exact percentage of relaxation state of the InGaN layer and the mechanism of relaxation that is involved.

SUMMARY AND CONCLUSIONS

In summary, InGaN/GaN core−shell structures with a single wide InGaN quantum well (SQW) were grown on arrays of etched GaN nanorods. EDX measurements of the QW confirmed a difference of InN homogeneity on the $\{1\bar{1}01\}$ planes compared with the *m*-planes. Nanoscale-range compositional fluctuations, with regions of higher and lower InN fraction, were found in the InGaN well on the *m*-plane, while the InGaN well on the $\{1\bar{1}01\}$ plane was uniform. The long-range InN fraction integrated on the *m*-plane SQW, from the top to the bottom of the nanorods led to a variation of just 7 meV·μm^{-1} in the layer grown at 750 °C, but increased to 40 meV·μm^{-1} at a growth temperature of 650 °C. Optical characterization demonstrated that homogeneous emission arose from the *m*-plane despite the short-range inhomogeneity within the QW. Finally, a comparison between calculated InN

DOI: 10.1021/acs.cgd.5b01438
Cryst. Growth Des. 2016, 16, 1907−1916

fraction from the emission peak and measured InN fraction indicated that the *m*-plane InGaN was partially relaxed, likely due to elastic relaxation since no misfit dislocations were seen in HRTEM.

To conclude, recent reviews of InGaN/GaN core−shell nanorods have highlighted the challenge and importance of controlling the long-range homogeneity along the length of the rod.[1,43] The results presented in this paper show that wide InGaN/GaN SQWs of uniform width and nearly uniform volume-averaged composition can be grown over the entire ∼1.2 μm length of *m*-planes created from etched GaN cores arranged in a hexagonal array of 2 μm pitch. However, nanoscale fluctuations of slightly raised InN mole fraction of up to 2−2.5 atom % occur in the InGaN layer, spaced at 20−30 nm intervals. Such excellent *m*-plane coverage by the InGaN shell was obtained for growth temperatures in the range 650−750 °C on etched GaN cores demonstrating the existence of a wide growth parameter space for designing epitaxial InGaN/GaN core−shell NRs with near-uniform average emission wavelength from the *m*-plane sidewalls. Adopting a nanorod pitch of 2 μm and simultaneously reducing the fill factor from 27% (used in our previous work) to 12% have contributed to the reported high uniformity in the *m*-plane optical emission. As such, these results conform to InGaN growth on three-dimensional multifaceted structures proceeding primarily by gas-phase diffusion.[44] Further work is required to determine the range of fill factors and pitch for which uniform composition can be achieved. Fundamentally this work shows that long-range homogeneity is achievable with the right NR array geometry.

EXPERIMENTAL DETAILS

A nickel-based metal mask of thickness 200 nm was created using a nanoimprint lift-off technique.[45] This resulted in a hexagonal array of metal dots of ∼510 nm diameter with a 2000 nm pitch. The GaN/AlN/Si NR array was etched in an inductively coupled plasma (ICP) dry etch system (Oxford Instruments System 100 Cobra) using the following recipe: Cl_2 flow − 50 sccm, Ar flow − 10 sccm, RIE power − 120 W, ICP source power − 800 W, chamber pressure − 9 mTorr and temperature − 150 °C.[46]

The MOVPE GaN regrowth step comprised 6 min of GaN growth at 1000 °C and 100 mbar, using a TMGa flow rate of 8 sccm, a NH_3 flow rate of 5 slm, and H_2 carrier gas.

The InGaN shell growth parameters for the three samples were identical apart from the temperature: pressure −300 mbar, TMGa flow rate − 9 sccm, TMIn flow rate − 200 sccm, NH_3 flow rate − 5 slm, N_2 carrier gas. A GaN capping layer was grown on all samples with identical growth parameters for all samples: temperature − 900 °C, pressure − 100 mbar, TMGa flow rate − 8 sccm, NH_3 flow rate − 5 slm.

Samples for TEM were prepared by a dual beam focused ion beam system. The nanorods were protected by a platinum layer prior to etching to reduce the damage that could occur with the use of an ion beam system. The samples for EDX measurements and atomic resolution STEM were prepared by a tripod polishing method using an Allied Tech Multiprep unit. Specimens were then ion-milled with a Gatan Precision Ion Polishing System (PIPS) using 1.5−5 keV argon ions for further thinning and removing the residue of polishing contamination from the specimens. Atomic resolution STEM images were acquired using a FEI TITAN 80−300 microscope that was equipped with a CEOS CESCOR spherical aberration (Cs) corrector in the probe forming lens and high-brightness FEI XFEG electron source. Atomic resolution HAADF STEM images were acquired at an accelerating voltage of 300 keV and probe convergence semiangle of 17.9 mrad and collection semiangle of 55−200 mrad. Energy dispersive X-ray spectroscopy analyses were carried out using FEI Tecnai Osiris. This microscope was equipped with XFEG and Super X system EDS detectors. This detector comprises four Bruker silicon drift detectors (SDD) arranged symmetrically around the optic axis of the microscope for high collection efficiency and high count rate. Spectrum images were acquired at a spatial sampling of 2 nm/pixel and 200 ms/pixel dwell times with a probe current of approximately 0.5 nA, at an accelerating voltage of 200 keV. Using principal component analysis (PCA) and independent component analysis (ICA) (implemented in HyperSpy[47]), two independent and uncorrelated components were identified in the spectrum images. The first component contains Ga and N X-ray peaks, and the second component contains Ga, In, and N X-ray peaks. To obtain the composition of the InGaN shell, the intensities of Ga K_α and In L_α peaks were quantified using the Cliff-Lorimer method and the *k*-factor provided by the manufacturer of the EDX system (Bruker). The errors were also estimated from Poisson statistics. The ICA technique is capable of differentiating true spectra from the underlying noise efficiently, and, as a result, noisy spectra can be tolerated. Using the ICA technique, the required sample beam dose was therefore significantly minimized without compromising the accuracy of quantification.

High-resolution cathodoluminescence (CL) hyperspectral imaging measures the full emission spectrum from successive localized regions determined by the probing volume of a scanning electron beam in order to build up a multidimensional data set containing spatial and spectroscopic information on the sample. The measurements were carried out at room temperature in a modified FEI Quanta 250 field-emission SEM with an accelerating voltage of 5 keV and had a spatial step size of 20 nm. Light was collected using an NA0.28 reflecting objective with its axis perpendicular to the electron beam and focused directly to the entrance of the spectrograph using an off-axis paraboloidal mirror. We used a 125 mm focal length spectrograph with a 600 lines/mm grating and 50 μm entrance slit, coupled to a cooled electron multiplying charge-coupled device (EMCCD) detector. Further details of the experimental setup can be obtained from ref 40.

In order to determine a value for the InN fraction for the samples grown at 700 and 650 °C, the mean value of multiple EDX maps close to the center of the QW was calculated. These maps came from the top, middle, and bottom of the *m*-plane. The standard errors on the mean value were all below 0.06 atom %. These errors can be neglected when compared with the experimental/instrumental error of 1.4 atom % and 2.0 atom % associated with the EDX measurements for the sample grown at 700 and 650 °C respectively. Therefore, the InN fraction and emission peak from the *m*-plane was determined as 10.3 ± 1.4 atom % and 3.02 ± 0.03 eV for the sample grown at 700 °C, and 18.6 ± 2.0 atom % and 2.61 eV ± 0.05 eV, for the sample grown at 650 °C.

AUTHOR INFORMATION

Corresponding Authors

*(E.D.L.) E-mail: E.Le.Boulbar@bath.ac.uk.

*(P.A.S.) E-mail: p.shields@bath.ac.uk.

Present Address

#Department of Chemistry, University of Waterloo, 200 University Avenue, Waterloo, Ontario, Canada, N2L 3G1. E-mail: svajarga@uwaterloo.ca.

Author Contributions

▽E.D.L., P.R.E., S.H.V., and P.A.S. contributed equally.

Funding

Financial support is acknowledged from the EPSRC, UK via Grant No. EP/I012591/1 "Lighting the Future" and Grant No. EP/M015181/1, "Manufacturing nano-GaN". C.R.B. acknowledges European Union's Seventh Framework Programme (FP/2007−2013)/ERC Grant Agreement No. 320963 on Novel Energy Materials, Engineering Science and Integrated Systems (NEMESIS).

DOI: 10.1021/acs.cgd.5b01438
Cryst. Growth Des. 2016, 16, 1907−1916

Notes

The authors declare no competing financial interest.
This publication is supported by multiple datasets, which are openly available at locations cited in the reference section.

■ ACKNOWLEDGMENTS

The authors would like to thank OSRAM Opto Semiconductors GmbH for the provision of the GaN/silicon templates.

■ REFERENCES

(1) Mandl, M.; Wang, X.; Schimpke, T.; Kölper, C.; Binder, M.; Ledig, J.; Waag, A.; Kong, X.; Trampert, A.; Bertram, F.; Christen, J.; Barbagini, F.; Calleja, E.; Strassburg, M. *Phys. Status Solidi RRL* **2013**, *7*, 800−814.
(2) Koester, R.; Sager, D.; Quitsch, W.-A.; Pfingsten, O.; Poloczek, A.; Blumenthal, S.; Keller, G.; Prost, W.; Bacher, G.; Tegude, F.-J. *Nano Lett.* **2015**, *15*, 2318−2323.
(3) Tchernycheva, M.; Messanvi, A.; de Luna Bugallo, A.; Jacopin, G.; Lavenus, P.; Rigutti, L.; Zhang, H.; Halioua, Y.; Julien, F. H.; Eymery, J.; Durand, C. *Nano Lett.* **2014**, *14*, 3515−3520.
(4) Liao, C.-H.; Chang, W.-M.; Yao, Y.-F.; Chen, H.-T.; Su, C.-Y.; Chen, C.-Y.; Hsieh, C.; Chen, H.-S.; Tu, C.-G.; Kiang, Y.-W.; Yang, C. C.; Hsu, T.-C. *J. Appl. Phys.* **2013**, *113*, 054315.
(5) Chang, J.-R.; Chang, S.-P.; Li, Y.-J.; Cheng, Y.-J.; Sou, K.-P.; Huang, J.-K.; Kuo, H.-C.; Chang, C.-Y. *Appl. Phys. Lett.* **2012**, *100*, 261103.
(6) Ra, Y.-H.; Navamathavan, R.; Kang, S.; Lee, C.-R. *J. Mater. Chem. C* **2014**, *2*, 2692.
(7) Yu, Z.; Yang, Z.; Wang, S.; Jin, Y.; Liu, J. G.; Gong, M.; Sun, X. *Chem. Vap. Deposition* **2005**, *11*, 433−436.
(8) Kuykendall, T. R.; Altoe, M. V. P.; Ogletree, D. F.; Aloni, S. *Nano Lett.* **2014**, *14*, 6767−6773.
(9) Salomon, D.; Dussaigne, A.; Lafossas, M.; Durand, C.; Bougerol, C.; Ferret, P.; Eymery, J. *Nanoscale Res. Lett.* **2013**, *8*, 61.
(10) Tessarek, C.; Dieker, C.; Spiecker, E.; Christiansen, S. *Jpn. J. Appl. Phys.* **2013**, *52*, 08JE09.
(11) Koester, R.; Hwang, J. S.; Durand, C.; Le Si Dang, D.; Eymery, J. *Nanotechnology* **2010**, *21*, 015602.
(12) Coulon, P.-M.; Mexis, M.; Teisseire, M.; Jublot, M.; Vennéguès, P.; Leroux, M.; Zuniga-Perez, J. *J. Appl. Phys.* **2014**, *115*, 153504.
(13) Liao, C.-H.; Tu, C.-G.; Chang, W.-M.; Su, C.-Y.; Shih, P.-Y; Chen, H.-T.; Yao, Y.-F; Hsieh, C.; Chen, H.-S.; Lin, C.-H.; Yu, C.-K.; Kiang, Y.-W.; Yang, C. C. *Opt. Express* **2014**, *22*, 1874−1881.
(14) Bae, S.; Jung, B. O.; Lekhal, K.; Kim, S. Y.; Lee, J. Y.; Lee, D.; Deki, M.; Honda, Y.; Amano, H. *CrystEngComm* **2016**, *18*, 1505; *CrystEngComm* **2016**, *18*, 1505.
(15) Hersee, S. D.; Sun, X.; Wang, X. *Nano Lett.* **2006**, *6*, 1808−1811.
(16) Bergbauer, W.; Strassburg, M.; Kölper, Ch.; Linder, N.; Roder, C.; Lähnemann, J.; Trampert, A.; Fündling, S.; Li, S. F.; Wehmann, H.-H.; Waag, A. *Nanotechnology* **2010**, *21*, 305201.
(17) Li, S. F.; Fuendling, S.; Wang, X.; Merzsch, S.; Al-Suleiman, M. A. M.; Wei, J. D.; Wehmann, H.-H.; Waag, A.; Bergbauer, W.; Strassburg, M. *Cryst. Growth Des.* **2011**, *11*, 1573−1577.
(18) Chen, X. J.; Hwang, J. S.; Perillat-Merceroz, G.; Landis, S.; Martin, B.; Le Si Dang, D.; Eymery, J.; Durand, C. *J. Cryst. Growth* **2011**, *322*, 15−22.
(19) Choi, K.; Arita, M.; Arakawa, Y. *J. Cryst. Growth* **2012**, *357*, 58−61.
(20) Coulon, P.-M.; Alloing, B.; Brändli, V.; Lefebvre, D.; Chenot, S.; Zúñiga-Pérez. *Phys. Status Solidi B* **2015**, *252*, 1096−1103.
(21) Wang, X.; Li, S.; Mohajerani, M. S.; Ledig, J.; Wehmann, H.; Mandl, M.; Strassburg, M.; Steegmüller, U.; Jahn, U.; Lähnemann, J.; Riechert, H.; Griffiths, I.; Cherns, D.; Waag, A. *Cryst. Growth Des.* **2013**, *13*, 3475−3480.
(22) Le Boulbar, E. D.; Gîrgel, I.; Lewins, C. J.; Edwards, P. R.; Martin, R. W.; Šatka, A.; Allsopp, D. W. E.; Shields, P. A. *J. Appl. Phys.* **2013**, *114*, 094302.
(23) Wang, G. T.; Li, Q.; Wierer, J. J.; Koleske, D. D.; Figiel, J. *Phys. Status Solidi A* **2014**, *211*, 748−751.
(24) Lewins, C. J.; Le Boulbar, E. D.; Lis, S. M.; Edwards, P. R.; Martin, R. W.; Shields, P. A.; Allsopp, D. W. E. *J. Appl. Phys.* **2014**, *116*, 044305.
(25) Griffiths, I.; Cherns, D. Dataset for Structural and optical emission uniformity of m-plane InGaN single quantum wells in core-shell nanorods. University of Bath, 2016, http://doi.org/10.15125/BATH-00150.
(26) Hosseini Vajargah, S.; Humphreys, C. J. Dataset for Structural and optical emission uniformity of m-plane InGaN single quantum wells in core-shell nanorods. University of Bath, 2016, http://doi.org/10.15125/BATH-00150.
(27) Brounkov, P. N.; Polimeni, A.; Stoddart, S. T.; Henini, M.; Eaves, L.; Main, P. C.; Kovsh, A. R.; Musikhin, Y. G.; Konnikov, S. G. *Appl. Phys. Lett.* **1998**, *73*, 1092−1094.
(28) Koester, R.; Hwang, J.-S.; Salomon, D.; Chen, X.; Bougerol, C.; Barnes, J.-P.; Le Si Dang, D.; Rigutti, L.; de Luna Bugallo, A.; Jacopin, G.; Tchernycheva, M.; Durand, C.; Eymery, J. *Nano Lett.* **2011**, *11*, 4839−4845.
(29) Kelchner, K. M.; Kuritzky, L. Y.; Nakamura, S.; DenBaars, S. P.; Speck, J. S. *J. Cryst. Growth* **2015**, *411*, 56−62.
(30) Kelchner, K. M.; Kuritzky, L. Y.; Fujito, K.; Nakamura, S.; DenBaars, S. P.; Speck, J. S. *J. Cryst. Growth* **2013**, *382*, 80−86.
(31) Wernicke, T.; Schade, L.; Netzel, C.; Rass, J.; Hoffmann, V.; Ploch, S.; Knauer, A.; Weyers, M.; Schwarz, U.; Kneissl, M. *Semicond. Sci. Technol.* **2012**, *27*, 024014.
(32) Edwards, P. R.; Martin, R. W. Dataset for Structural and optical emission uniformity of m-plane InGaN single quantum wells in core-shell nanorods. University of Strathclyde, 2016, http://dx.doi.org/10.15129/07d0319e-53b9-45ac-a46d-460b95ea2eda.
(33) Girgel, I.; Edwards, P. R.; Le Boulbar, E. D.; Coulon, P.-M.; Sahonta, S.-L.; Allsopp, D. W. E.; Martin, R. W.; Humphreys, C. J.; Shields, P. A. *J. Nanophotonics* **2016**, *10* (1), 016010.
(34) Stankevič, T.; Mickevičius, S.; Schou Nielsen, M.; Kryliouk, O.; Ciechonski, R.; Vescovi, G.; Bi, Z.; Mikkelsen, A.; Samuelson, L.; Gundlach, C.; Feidenhans'l, R. *J. Appl. Crystallogr.* **2015**, *48*, 344−349.
(35) Zhuang, Y. D.; Bruckbauer, J.; Shields, P. A.; Edwards, P. R.; Martin, R. W.; Allsopp, D. W. E. *J. Appl. Phys.* **2014**, *116* (17), 174305.
(36) Böcklin, C.; Veprek, R. G.; Steiger, S.; Witzigmann, B. *Phys. Rev. B: Condens. Matter Mater. Phys.* **2010**, *81*, 155306.
(37) Strite, S.; Morko, H. *J. Vac. Sci. Technol., B: Microelectron. Process. Phenom.* **1992**, *10*, 1237−1266.
(38) De Luna Bugallo, A.; Rigutti, L.; Jacopin, G.; Julien, F. H.; Durand, C.; Chen, X. J.; Salomon, D.; Eymery, J.; Tchernycheva, M. *Appl. Phys. Lett.* **2011**, *98*, 233107.
(39) Coulon, P.-M.; Hugues, M.; Alloing, B.; Beraudo, E.; Leroux, M.; Zúñiga-Pérez. *Opt. Express* **2012**, *20*, 18707−18716.
(40) Edwards, P. R.; Jagadamma, L. K.; Bruckbauer, J.; Liu, C.; Shields, P.; Allsopp, D.; Wang, T.; Martin, R. W. *Microsc. Microanal.* **2012**, *18*, 1212−1219.
(41) Orsal, G.; El Gmili, Y.; Fressengeas, N.; Streque, J.; Djerboub, R.; Moudakir, T.; Sundaram, S.; Ougazzaden, A.; Salvestrini, J. P. *Opt. Mater. Express* **2014**, *4*, 1030.
(42) Le Boulbar, E. D. Dataset for Structural and optical emission uniformity of m-plane InGaN single quantum wells in core-shell nanorods. University of Bath, 2016, http://doi.org/10.15125/BATH-00150.
(43) Eymery, J.; Le Si Dang, D. In *Modeling, Characterization and Production of Nanomaterials*; Tewary,V., Zhang,Y., Eds; A Volume in Woodhead Publishing Series in Electronic and Optical Materials; Elsevier: Amsterdam, 2015; Vol. *73*, pp 323−335, http://doi:10.1016/B978-1-78242-228-0.09992-0.
(44) Fang, H.; Yang, Z. J.; Wang, Y.; Dai, T.; Sang, L. W.; Zhao, L. B.; Yu, T. J.; Zhang, G. Y. *J. Appl. Phys.* **2008**, *103*, 014908.

DOI: 10.1021/acs.cgd.5b01438
Cryst. Growth Des. 2016, 16, 1907−1916

(45) Shields, P. A.; Allsopp, D. W. E. *Microelectron. Eng.* **2011**, *88*, 3011−3014.
(46) Shields, P. A.; Hugues, M.; Zúñiga-Pérez, J.; Cooke, M.; Dineen, M.; Wang, W.; Causa, F.; Allsopp, D. *Phys. Status Solidi* **2012**, *9*, 631−634.
(47) De la Pena, F., Burdet, P., Sarahan, M., Nord, M., Ostasevicius, T., Taillon, J., Eljarrat, A., Mazzucco, S., Fauske, V. T., Donval, G., Zagonel, L. F., Iyengar, I., Walls, M. *hyperspy: HyperSpy 0.8*; Zenodo, 2015, http://dx.doi.org/10.5281/zenodo.16850.

DOI: 10.1021/acs.cgd.5b01438
Cryst. Growth Des. 2016, 16, 1907−1916